Optics Letters

Twist-engineered phonon polaritons in $\alpha - V_2O_5$

H. Shiravi,[1,2] W. Zheng,[1,2] Y. He,[3] S. Ran,[4] D. A. Rhodes,[3,5] L. Balicas,[1,2] H. D. Zhou,[6] and G. X. Ni[1,2,*]

[1]Department of Physics, Florida State University, Tallahassee, Florida 32306, USA
[2]National High Magnetic Field Laboratory, Tallahassee, Florida 32310, USA
[3]Department of Materials Science and Engineering, University of Wisconsin-Madison, Madison, Wisconsin 53706, USA
[4]Department of Physics, Washington University in St. Louis, St. Louis, Missouri 63130, USA
[5]Department of Physics, University of Wisconsin-Madison, Madison, Wisconsin 53706, USA
[6]Department of Physics and Astronomy, University of Tennessee, Knoxville, Tennessee 37996, USA
*guangxin.ni@magnet.fsu.edu

Received 21 January 2025; revised 30 March 2025; accepted 31 March 2025; posted 4 April 2025; published 29 April 2025

The advent of layered materials has unveiled new opportunities for tailoring electromagnetic waves at the subwavelength scale, particularly through the study of polaritons, a hybrid light–matter excitation. In this context, twist-optics, which investigates the optical properties of twisted stacks of van der Waals (vdW) layered specimens, has emerged as a powerful tool. Here, we explore the tunability of phonon polaritons in α-V_2O_5 via interlayer twisting using scanning nano-infrared (IR) imaging. We show that the polaritonic response can be finely adjusted by varying their interlayer electromagnetic coupling, allowing for precise control over the propagation direction and phase transition from open unidirectional iso-frequency contours to closed elliptic geometries. Our experimental results, in conjugate with theoretical modeling, reveal the mechanisms underpinning this tunability, highlighting the role of twist-induced nano-light modifications for advanced nanophotonic control at the nanoscale.

https://doi.org/10.1364/OL.557267

Twisted moiré heterostructures, created by stacking two layers of two-dimensional (2D) van der Waals (vdW) materials on top of each other with a relative twist angle (θ), have revealed a multitude of extraordinary physical phenomena [1–5]. In twisted electronics, tremendous progress has been achieved based on graphene and transition metal dichalcogenides (TMD) structures, with exotic discoveries ranging from superconductivity, correlated insulating states, ferromagnetism, and fractional quantum anomalous Hall effects [6–9]. In twisted optics and photonics, efforts have expanded across a wide range of frequencies, from the visible to IR, where moiré excitons in TMDs, nanoscale photonic crystals, and novel features in surface plasmon/phonon polaritons in twisted graphene systems and polar insulators have been realized [4,5,10–12]. These achievements have also spurred the exploration of surface polaritons in twisted structures to manipulate and control long-wavelength electromagnetic fields down to the nanoscale [5–16].

A notable example is the observation of topological transitions and the canalized phonon polariton in twisted α-MoO_3 with highly directional propagation around 60° twist angles [5,17–21]. In contrast to traditional polaritonic media, such as hBN or graphene-based heterostructures, the canalized flat polariton dispersion along a specific direction would enables efficient energy transfer with minimal spatial spreading. Despite these achievements, twisted-polaritonics in polar insulating systems remains in its early stage [5,19,22], particularly in identifying systems that support the propagation of canalized polaritons with enhanced tunability, broader spectral coverage, and optimized propagation efficiency. Identifying new twisted vdW heterostructures capable of supporting canalized polaritons thus offers the potential to address existing limitations while unlocking new functionalities in nano-polaritonic technologies across different frequency domains.

We report the direct observation of tunable phonon polariton transitions in twisted α-V_2O_5 using scattering-type scanning near-field optical microscopy (s-SNOM), which enables local optical excitations of the phonon resonance states at selected long-wavelength IR frequencies [23–26]. We show that twisted α-V_2O_5 hosts propagating polaritons that are tunable in the mid-IR wavelengths from $\lambda_{IR} \sim 11.1$–11.6 μm [13]. The distinct dielectric permittivity, ϵ, of α-V_2O_5 along the three crystalline axes, as determined from previous far-field measurements, confirms the existence of three Reststrahlen bands (RB) and the corresponding phonon polaritons with them (see Supplement 1) [26]. In our studies, we focus on such hyperbolic frequency regime of RB_2 ($\omega \sim 860$–$900\ cm^{-1}$) where $\epsilon_a<0$, $\epsilon_{bc}>0$, respectively. Given the strong anisotropic in-plane ϵ in RB_2 and interlayer hybridization of twisted α-V_2O_5, our observation indicates a phonon polariton transitions can be detected, which, depending on the interlayer twist angle, manifests either as unidirectional canalized or closed elliptical propagations. The continuous variation in polariton wavefront geometries, along with the quantitative agreement with electromagnetic modeling, suggests that twisted α-V_2O_5 holds promise for developing tunable IR polaritonic devices with potential applications in nanophotonic and optoelectronics.

To access the phonon polaritons in α-V_2O_5, we performed nano-IR imaging using s-SNOM based on a tapping-mode

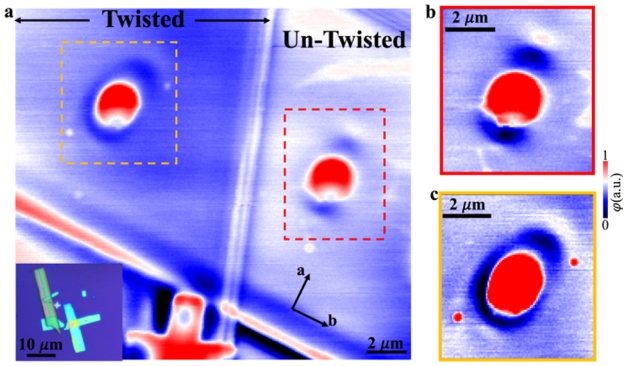

Fig. 1. Nano-IR imaging of twisted versus untwisted α-V_2O_5 flake within the same field-of-view. (a) Large-scale near-field imaging of α-V_2O_5 heterostructure, with the left region representing the twisted regime and the right region showing the untwisted regime. The inset shows the optical image of the SNOM tip and the α-V_2O_5 device under study. (b), (c) Zoomed-in near-field phase $\phi(\omega)$ images as marked in the panel at the incident light frequency of 860 cm^{-1} (~106 meV). Distinct phonon polariton wavefronts are observed around the pre-patterned Au micro-disk (with a diameter of ~2 μm) on top of the α-V_2O_5 flakes.

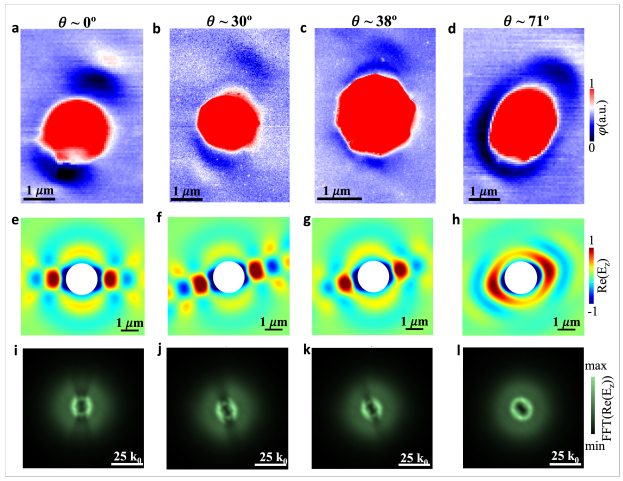

Fig. 2. Nano-IR images with varying twist angles at $\omega = 860\ cm^{-1}$. (a)–(d) Experimentally measured near-field images of four different α-V_2O_5 devices with interlayer twist angles of $\theta = 0°$ (panel (a)), $\theta = 30°$ (panel (b)), $\theta = 38°$ (panel (c)), and $\theta = 70°$ (panel (d)), respectively. (e)–(h) Theoretically simulated $Re(E_z)$ images showing the variation of the polariton wavefront at the same twist angles as in panels (a)–(d). The agreement between the calculated $Re(E_z)$ and the experimental results underscores the importance of interlayer polariton coupling. (i)–(l) corresponding FFT images of panels shown in (e)–(h). The scale-bar in (i)–(l) is 25 k_0.

atomic force microscope (AFM) equipped with a metallic tip (Fig. 1(a) inset). The AFM tip with a radius of ~20 nm, and oscillation frequency of 300 KHz with an amplitude of 80 nm, was illuminated by IR light with frequency $\omega = 2\pi/\lambda_{IR}$, generating a strongly enhanced local electric field underneath. This setup resolves the problem of photon–phonon momentum mismatch [27–31], enabling the launch of phonon polariton waves with wavelength $\lambda_p \ll \lambda_{IR}$ [5,17,18,32–34]. The local electric field of the phonon polariton waves gets scattered into the far-field by the sample edge, enabling direct measurement of the polaritonic response with the ~20 nm spatial resolution.

Representative nano-IR imaging data is depicted in Fig. 1, where we show the near-field image for $\omega = 860\ cm^{-1}$ and a 100-nm-thick α-V_2O_5 flake. To excite phonon polaritons, we define gold disks as a local phonon polariton launcher on top of the α-V_2O_5 flake to produce propagating phonon polariton waves upon IR illumination. We first focus on phonon polaritons in a thin layer of α-V_2O_5 without twisting (Fig. 1(b)). Clearly, the detected polaritonic features around the Au disk do not propagate outward symmetrically. Instead, we observe a very clear directionality in the RB_2 frequencies. Such unidirectional polariton propagation in the RB_2 frequencies indicates a canalized wavefront in pristine α-V_2O_5 flakes, reminiscent of previous polariton canalization observations in twisted α-MoO_3 or the dielectric engineering-induced canalization in Li-intercalated V_2O_5 [14].

In sharp contrast to the unidirectional polaritonic wavefront discussed above, for the same flake but adding another thin layer of α-V_2O_5 with a relative twist angle of 71°, we see the formation of elliptic polariton wave pattern, as shown in Fig. 1(c) (see Supplement 1). The smallest wavelength is parallel to the [010] (*b*-axis), while the largest wavelength is along [100] (*a*-axis). These elliptic polaritons are reminiscent of earlier observations in other polar insulators [18,35–37]. We note that such polariton wave pattern variation as a function of interlayer twist angle could not be explained by increasing the thickness of α-V_2O_5, which would simply increase the polariton wavelength rather than modify the wave pattern. Instead, these observations suggest that the interlayer coupling between the two branches of the polariton dispersion likely drives the transition of the wavefront from a unidirectional, canalized geometry to an elliptic one, as detailed below.

To systematically examine the twist angle dependence of the phonon polariton coupling between two adjacent α-V_2O_5 crystals, we conducted nano-IR imaging studies on multiple devices with different interlayer twist angles (Figs. 2(a)–2(d)). At $\theta = 0°$, the wavefront propagates along the *a*-axis, which we use as our reference point to compare with other twist angles. As their interlayer twist angle increases, we observe a gradual rotation and transformation of the wavefront. At $\theta = 30°$, the wavefront largely retains its unidirectional propagation, albeit the propagating direction shows a noticeable rotation/deviation from the $\theta = 0°$ case. This deviation becomes more pronounced at $\theta \sim 38°$, where we observe not only the unidirectional polariton wavefront but also a further shift in propagation direction relative to the zero-twist angle. However, at $\theta \sim 70°$, a closed wavefront emerges around the Au launcher, signaling the completion of the polariton phase transition from an open, canalized geometry to the closed, elliptic wave structure. Clearly, a polariton phase transition is accompanied as a function of twist angles, as detailed below.

Our study of the phonon polariton dependence on interlayer twist angle is well captured by the numerical simulations. To verify the experimental observations, we performed full-wave simulations (see Supplement 1) at variable twist angles for α-V_2O_5, examining the real part of the *z*-component of the electric field ($Re(E_z)$). The experimentally determined dielectric permittivity tensor was used as the input parameter [38] (see Supplement 1). By plotting the calculated $Re(E_z)$ (Figs. 2(e)–2(h)), we demonstrate similar electric field distribution transitions, from a closed to an open wavefront with an increasing twist angle. The same trend is reflected in the Fourier

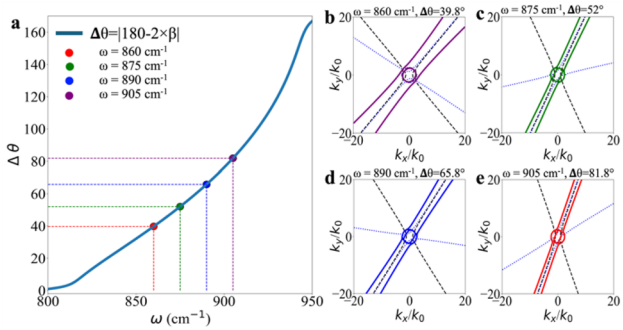

Fig. 3. Analytical calculations for determining critical angles at different frequencies. (a) Variation of the critical angle as a function of frequency. (b)–(e) Dispersion diagrams at different frequencies with their corresponding critical twist angles: (b) $\omega = 860\,\mathrm{cm}^{-1}$, $\theta = 39.7°$; (c) $\omega = 875\,\mathrm{cm}^{-1}$, $\theta = 52.0°$; (d) $\omega = 890\,\mathrm{cm}^{-1}$, $\theta = 65.8°$; (e) $\omega = 905\,\mathrm{cm}^{-1}$, $\theta = 81.8°$. The black dashed lines represent the original coordinate system (bottom layer), while the blue dotted lines denote the rotated system (top layer).

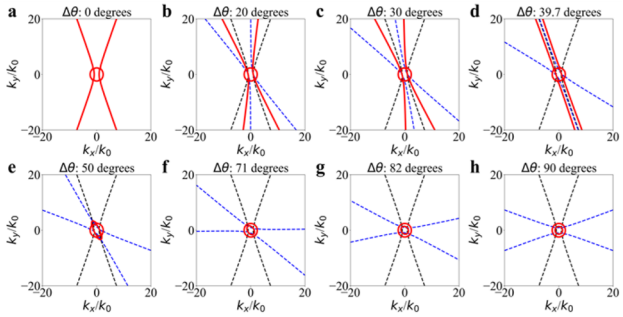

Fig. 4. Analytical dispersion diagrams of twisted α-V_2O_5 at a frequency of $860\,\mathrm{cm}^{-1}$. (a)–(h) Dispersion diagrams for devices with interlayer twist angles at $\theta = 0°$ (panel a), $\theta = 20°$ (panel b), $\theta = 30°$ (panel c), $\theta = 40°$ (panel d), $\theta = 50°$ (panel e), $\theta = 71°$ (panel f), $\theta = 82°$ (panel g), and $\theta = 90°$ (panel h), respectively. The black dashed lines represent the dispersion of the bottom layer, which remains unrotated. The blue dashed lines correspond to the dispersion of the top layer after rotation, while the red solid line indicates the resulting final dispersion.

spectrum, as shown in Figs. 2(i)–2(l). Briefly, at small twist angles ($\theta < 30°$), the field pattern remains largely identical, although the polariton propagation direction rotates continuously as a function of the interlayer twist angle (Figs. 2(e)–2(f)). Increasing the twist angle from $\theta \sim 30°$ to 38° not only slightly rotates the polariton propagation direction but also modifies the electrical field pattern. Beyond the critical angle, however, the polariton wavefront transforms into an elliptic geometry (see Supplement 1). These findings validate our observed polariton wavefront transformation triggered by the interlayer phonon polariton coupling initiated by the relative twist angle between the adjacent two layers.

Physically, the critical angle marks the boundary between hyperbolic and elliptical wavefronts. At this threshold, perfect canalization is expected, signifying a phase transition from open to closed polariton wave behavior. Because the permittivity values ε_x and ε_y vary with frequency, the open angle $\beta = \tan^{-1}\left(\sqrt{-\varepsilon_x/\varepsilon_y}\right)$ and the critical angle, defined as $\Delta\theta = |180° - 2 \times \beta|$, are also frequency dependent. Figure 3(a) illustrates the variation of $\Delta\theta$ across frequencies, calculated numerically at $\omega = 860$, 875, 890, and $905\,\mathrm{cm}^{-1}$, alongside their associated polariton dispersion (Figs. 3(b)–3(e)). For instance, at $\omega = 860\,\mathrm{cm}^{-1}$, perfect canalization occurs at a twist angle of 39.7°, aligning with our experimental results in Fig. 2. At higher frequencies, $\Delta\theta$ increases, approaching 90° at the edge of the RB_2 frequency regime.

To gain deeper insight into the critical angle of the observed polariton transition, we further conducted analytical studies by solving the source-free Maxwell equations to derive the polariton dispersion for each α-V_2O_5 flake, modeled as a 2D sheet. Interlayer coupling was represented by positioning the top flake directly above the bottom flake with an infinitesimal separation. For untwisted α-V_2O_5 (Fig. 4(a)), the hyperbolic dispersion of phonon polariton propagates at the open angle β [5,39]. Upon introducing a relative twist between layers (Figs. 4(b) and 4(c)), the polariton dispersion of the fixed bottom layer diverges from that of the top layer, resulting in a rotation of the overall dispersion diagram. Consequently, the two branches of the total dispersion become increasingly parallel to one another. Around the critical angle of $\Delta\theta \sim 40°$ (Fig. 4(d)), the dispersion diagram shows two perfectly parallel lines, indicative of an idealized polariton canalization in real-space imaging. Beyond this critical twist angle, the overall dispersion transitions from hyperbolic to elliptical wavefront, as shown in Figs. 4(e)–4(h). Another way to examine the polariton phase transition is through the number of anti-crossing points in their associated hybrid dispersions[13]. For instance, there are two anti-crossing points below the critical angle and four anti-crossing points above it (see Supplement 1). In short, both our numerical and analytical studies reproduce the experimental results, highlighting the good agreement between theory and observation.

We now discuss the possible mechanisms underlying the observed canalized phonon polariton propagation at the zero-twist angle and the associated phase transition in the relevant frequency range. One plausible explanation is the large β dictated by the highly anisotropic dielectric function of α-V_2O_5 flakes (see Supplement 1). For instance, at $\omega = 830\,\mathrm{cm}^{-1}$, β approaches 90°, corresponding to hyperbolic dispersion extending further along the principal directions and effectively narrowing the pathways for group velocity. Therefore, this expanded angular range facilitates polariton propagation in more collimated or nearly "canalized" wavefronts, even in the untwisted α-V_2O_5 flakes, characterized by highly confined energy flow. Such canalization effects can be further modulated via interlayer coupling through angle-dependent electromagnetic hybridization between anisotropic phonon polariton fields. For twisted α-V_2O_5 flakes, the effective interaction between two hyperbolic bands leading to anti-crossing behavior (Fig. 4), which further flattens the dispersion and induces relative rotation of the overall dispersion diagram across a wide range of $\Delta\theta$. Our dispersion analysis confirms that this tunability arises from the electromagnetic nature of the twisting tunability of phonon polaritons has been confirmed by our dispersion analysis of phonon polariton dispersions. This phenomenon highlights the pivotal role of twist-induced interlayer interactions in enhancing polariton confinement and tunability.

In short, we have demonstrated a tunable polariton phase transition in twisted α-V_2O_5 heterostructures. The observed variation in dispersion contours, transitioning from canalized to elliptic wavefront geometries in the mid-IR range, benefits from

the material's highly anisotropic property and effective electromagnetic interlayer coupling. Our systematic explorations of twist angle and frequency dependencies, supported by comprehensive theoretical modeling and simulations, underscore the transformative potential of polar oxides for advancing nanophotonics and polaritonics through twisting engineering. These findings suggest that similar effects in other related vdW materials could enable the design of programmable polaritonic properties [40,41], leveraging twisting to tailor functionalities across the technologically important mid-IR to far-IR spectrum at the nanoscale.

Funding. U.S. Department of Energy (DE-SC0022022, DE-SC0020254); Division of Materials Research (DMR-2145074, DMR-1644779, DMR-1644779, DMR-2236528, DMR-2309000, DMR 2219003); American Chemical Society Petroleum Research Fund (PRF# 66465-DNI10).

Acknowledgment. The near-field nano-optical imaging studies are supported by the U.S. Department of Energy (DOE) Early Career Research Program through the Office of Science, Basic Energy Sciences (BES), under award DE-SC0022022 (N.G.X.). Research on 2D polaritonics is supported by the National Science Foundation (NSF) CAREER award, under award DMR-2145074 (N.G.X.). N.G.X. acknowledges the support from ACS-DNI (PRF# 66465-DNI10). The National High Magnetic Field Laboratory is supported by the National Science Foundation through NSF/DMR-2128556 and the state of Florida. The crystal growth in UTK was supported by the U.S. Department of Energy with Grants No. DE-SC0020254. L.B. acknowledges support from the USNSF-DMR 2219003 (heterostructure fabrication) and the Office Naval Research DURIP Grant 11997003 (stacking under inert conditions). D.R. was supported by the NSF through the University of Wisconsin Materials Research Science and Engineering Center (DMR-2309000). The work at Washington University is supported by the National Science Foundation (NSF) Division of Materials Research Award DMR-2236528.

Disclosures. The authors declare no conflicts of interest.

Data availability. Data underlying the results presented in this paper may be obtained from the authors upon reasonable request.

Supplemental document. See Supplement 1 for supporting content.

REFERENCES

1. H. Park, J. Cai, E. Anderson, *et al.*, Nature **622**, 74 (2023).
2. M. Serlin, C. L. Tschirhart, H. Polshyn, *et al.*, Science **367**, 900 (2020).
3. Y. Cao, V. Fatemi, S. Fang, *et al.*, Nature **556**, 43 (2018).
4. S. S. Sunku, G. X. Ni, B. Y. Jiang, *et al.*, Science **362**, 1153 (2018).
5. G. Hu, Q. Ou, G. Si, *et al.*, Nature **582**, 209 (2020).
6. Z. Lu, T. Han, Y. Yao, *et al.*, Nature **626**, 759 (2024).
7. X. Wang and O. Vafek, Phys. Rev. X **14**, 021042 (2024).
8. Y. Zeng, Z. Xia, K. Kang, *et al.*, Nature **622**, 69 (2023).
9. C. N. Lau, M. W. Bockrath, K. F. Mak, *et al.*, Nature **602**, 41 (2022).
10. G. X. Ni, H. Wang, J. S. Wu, *et al.*, Nat. Mater. **14**, 1217 (2015).
11. S. Cui, J. Chengxin, Z. Zhen, *et al.*, Nano Lett. **24**, 11490 (2024).
12. J. Duan, G. Álvarez-Pérez, C. Lanza, *et al.*, Nat. Mater. **22**, 867 (2023).
13. J. Taboada-Gutiérrez, G. Álvarez-Pérez, J. Duan, *et al.*, Nat. Mater. **19**, 964 (2020).
14. A. I. F. Tresguerres-Mata, C. Lanza, J. Taboada-Gutiérrez, *et al.*, Nat. Commun. **15**, 2696 (2024).
15. Z. Zheng, F. Sun, W. Huang, *et al.*, Nano Lett. **20**, 5301 (2020).
16. J. Duan, N. Capote-Robayna, J. Taboada-Gutiérrez, *et al.*, Nano Lett. **20**, 5323 (2020).
17. W. Ma, P. Alonso-González, S. Li, *et al.*, Nature **562**, 557 (2018).
18. Z. Zheng, N. Xu, S. L. Oscurato, *et al.*, Sci. Adv. **5**, eaav8690 (2019).
19. M. Chen, X. Lin, T. H. Dinh, *et al.*, Nat. Mater. **19**, 1307 (2020).
20. Z. Zhou, R. Song, J. Xu, *et al.*, Nano Lett. **23**, 11252 (2023).
21. X. Jin and W. Luo, Opt. Mater. Express **14**, 2349 (2024).
22. H. Wang, A. Kumar, S. Dai, *et al.*, Nat. Commun. **15**, 69 (2024).
23. Z. Fei, G.-X. Ni, B.-Y. Jiang, *et al.*, ACS Photonics **4**, 2971 (2017).
24. M. E. Berkowitz, B. S. Y. Kim, G. Ni, *et al.*, Nano Lett. **21**, 308 (2020).
25. A. J. Frenzel, A. S. McLeod, D. Z.-R. Wang, *et al.*, Phys. Rev. B **97**, 035111 (2018).
26. H. Shiravi and G. X. Ni, Opt. Lett. **50**, 590 (2025).
27. S. S. Sunku, D. Halbertal, R. Engelke, *et al.*, Nano Lett. **21**, 1688 (2021).
28. G. X. Ni, A. S. McLeod, Z. Sun, *et al.*, Nature **557**, 530 (2018).
29. F. Hu, Y. Luan, M. E. Scott, *et al.*, Nat. Photonics **11**, 356 (2017).
30. H. Hu, N. Chen, H. Teng, *et al.*, Nat. Nanotechnol. **17**, 940 (2022).
31. H. Shiravi, A. Gupta, B. R. Ortiz, *et al.*, Nat. Commun. **15**, 5389 (2024).
32. S. Foteinopoulou, G. C. R. Devarapu, G. S. Subramania, *et al.*, Nanophotonics **8**, 2129 (2019).
33. G. Ni, A. S. McLeod, Z. Sun, *et al.*, Nano Lett. **21**, 5767 (2021).
34. G. Hu, W. Ma, D. Hu, *et al.*, Nat. Nanotechnol. **18**, 64 (2023).
35. P. Li, I. Dolado, F. J. Alfaro-Mozaz, *et al.*, Nano Lett. **17**, 228 (2017).
36. Z. Sun, A. Martinez, and F. Wang, Nat. Photonics **10**, 227 (2016).
37. T. Low, A. Chaves, J. D. Caldwell, *et al.*, Nat. Mater. **16**, 182 (2017).
38. H. N. S. Krishnamoorthy, Z. Jacob, E. Narimanov, *et al.*, Science **336**, 205 (2012).
39. G. Hu, A. Krasnok, Y. Mazor, *et al.*, Nano Lett. **20**, 3217 (2020).
40. Y. Ma, G. Zhong, Z. Dai, *et al.*, npj Nanophotonics **1**, 25 (2024).
41. W. Ma, G. Hu, D. Hu, *et al.*, Nature **596**, 362 (2021).